Scalable qubit architecture based on holes in quantum dot molecules

Sophia E. Economou,[1] Juan I. Climente,[2] Antonio Badolato,[3] Allan S. Bracker,[1] Daniel Gammon,[1] and Matthew F. Doty[4,*]

[1]*Naval Research Laboratory, Washington, DC 20375*

[2]*Departamento de Química Física i Analítica, Universitat Jaume I, E-12080 Castelló, Spain*

[3]*Department of Physics and Astronomy, University of Rochester, Rochester, New York 14627, USA*

[4]*Department of Materials Science and Engineering, University of Delaware, Newark, Delaware 19716, USA*

(Received 26 April 2012; revised manuscript received 12 July 2012; published 24 August 2012)

Spins confined in quantum dots are a leading candidate for solid-state quantum bits that can be coherently controlled by optical pulses. There are, however, many challenges to developing a scalable multibit information processing device based on spins in quantum dots, including the natural inhomogeneous distribution of quantum dot energy levels, the difficulty of creating all-optical spin manipulation protocols compatible with nondestructive readout, and the substantial electron-nuclear hyperfine interaction-induced decoherence. Here, we present a scalable qubit design and device architecture based on the spin states of single holes confined in a quantum dot molecule. The quantum dot molecule qubit enables a new strategy for optical coherent control with dramatically enhanced wavelength tunability. The use of hole spins allows the suppression of decoherence via hyperfine interactions and enables coherent spin rotations using Raman transitions mediated by a hole-spin-mixed optically excited state. Because the spin mixing is present only in the optically excited state, dephasing and decoherence are strongly suppressed in the ground states that define the qubits and nondestructive readout is possible. We present the qubit and device designs and analyze the wavelength tunability and fidelity of gate operations that can be implemented using this strategy. We then present experimental and theoretical progress toward implementing this design.

DOI: 10.1103/PhysRevB.86.085319 PACS number(s): 78.20.Ls, 78.47.−p, 78.55.Cr, 78.67.Hc

Single confined spins have long been considered as possible bit states for novel optoelectronic logic devices, including quantum computers.[1] Spins confined in III-V semiconductor self-assembled quantum dots (QDs) have received a great deal of attention because they interact strongly with light and provide the opportunity for ultrafast all-optical implementation of logic operations.[2–5] There has been dramatic progress in the initialization, coherent manipulation, and readout of single spins in GaAs and InGaAs QDs,[6–13] but many challenges to the creation of a scalable quantum logic device based on optical control of single spins remain. One serious obstacle is the natural inhomogeneous distribution of energy levels in a quantum dot ensemble. This distribution necessitates individually tuned lasers to control each bit and restricts the ability to mediate entanglement via photonic cavity modes.[14] Another obstacle is that existing approaches to all-optical coherent control of spins require a transverse magnetic field in order to mix spin states and permit Raman transitions.[8] The transverse magnetic field prevents nondestructive readout.[9] A third obstacle is the suppression of decoherence. Among the many channels for decoherence, the hyperfine interaction with nuclei is the most detrimental.[15–17]

We present a quantum bit (qubit) design and device architecture that overcomes many of these obstacles. In our approach, the two spin states of a single hole encode the qubit. The qubit hole is localized in the top QD of a coupled pair of vertically stacked InAs QDs. These stacked pairs of QDs are known as quantum dot molecules (QDMs) because coherent tunneling leads to the formation of states with delocalized wave functions that have molecular symmetries.[18–21] We propose initializing and rotating the spin using optically excited delocalized molecular states with mixed spin character. A different optically excited state that is immune to spin mixing provides a recycling transition for readout. We show that this approach enables all-optical coherent control of single hole spins, controlled interactions between two nonidentical qubits mediated by photonic cavity modes, and nondestructive readout of the spin projection along the growth axis.

The approach presented here builds on experimental progress in the coherent control of single hole spins[16,17,22–27] and electron spins in QDMs.[9] The new design combines advantages of these approaches and makes several key improvements that significantly enhance scalability. First, the hole spin is less sensitive to dephasing by hyperfine interactions with nuclei, which provide a dominant decoherence mechanism for electrons.[16,28] Second, the spin mixing for hole tunneling in QDMs can be engineered to be much larger than the mixing for electron tunneling, greatly enhancing the fidelity of the optically driven qubit rotation. Third, the spin mixing in QDMs provides a pathway to implement all-optical coherent control using only magnetic fields applied along the growth direction, which is parallel to the optical axis. As a result, the approach is compatible with the use of recycling transitions for nondestructive readout. Finally, our approach utilizes optical transitions between electrons and holes located in separate quantum dots. These transitions have an extremely large Stark shift as a function of applied electric fields, and thus provide an enhanced capacity to tune the transitions into resonance with external laser sources or optical cavity modes.

The use of "indirect" optical transitions, involving electrons and holes in separate QDs, underlies an important conceptual aspect of the device architecture proposed here. Existing device designs often assume an ensemble of identical QDs, which is impossible to achieve experimentally. Demonstrations of spin initialization, control, or readout using QDs typically identify the specific optical transitions of a particular QD

and then tune optical cavities and external laser sources into resonance with that particular QD. This approach cannot be scaled beyond a small number of qubits. In our approach we begin by accepting the inhomogeneous distribution of QD energy levels. We design a device architecture in which the optical transitions of a subset of individual QDMs within this ensemble can be tuned into resonance with a fixed-frequency optical cavity or external laser. The key to tuning many individual QDMs into resonance with a fixed-frequency optical cavity or laser is the use of indirect transitions whose energy shifts strongly with the electric field applied locally to individual QDMs.

We present detailed modeling of the QDM states that could be used for this scheme, compute the fidelity of gate operations implemented with this wavelength-tunable approach, and provide experimental evidence of the large spin mixing necessary for such a scheme. In Sec. I we present our qubit design and describe how this design suppresses hole-spin decoherence or dephasing in the logical basis states. In Sec. II we develop our strategies for full single-qubit all-optical control. We first analyze the use of indirect optical transitions (Sec. II A) and then describe how these indirect transitions enable single spin initialization and readout with enhanced wavelength tunability (Sec. II B). In Sec. II C we develop the coherent control of the hole spin using Raman transitions mediated by optically excited states with hole-spin mixing. In Sec. III we address scalability in the context of wavelength tunability and fidelity of spin control protocols and discuss how the conditional interactions can be mediated by photonic cavity modes. In Secs. IV and V we present progress toward the implementation of this device design, including experimental measurements of hole-spin mixing in the optically excited positive trion state and theoretical calculations of QDM structures that enhance the spin mixing.

I. QUBIT DESIGN

In Fig. 1(a) we schematically depict the band structure and lowest single particle energy levels for electrons and holes in the QDM designed for this application. The QDM grown by molecular beam epitaxy is embedded within a p-i-n diode structure that allows an applied electric field to tune the energy levels of the QDs relative to one another and the Fermi level. The bottom QD is truncated to a smaller height than the top QD so that the hole levels can be tuned into resonance while electron levels retain a significant energy offset that causes electrons to always relax to the top QD.[29] The tunnel barrier formed by the intrinsic GaAs region between the p-doped substrate and the bottom QD is chosen so that the QDM remains deterministically charged with a single hole in the electric field range of operation. Tunneling of electrons into the QDM is prevented by the inclusion of an $Al_xGa_{(1-x)}As$ ($x \leqslant 0.4$) blocking layer. The heterostructure design is schematically depicted in Fig. 1(d) and numerical values for the design are discussed in Appendix A.

Our qubit is defined by the spin projections along the growth axis of a single hole (h^+) confined in the QDM. The optically excited state has one additional electron-hole pair and is called a positive trion (X^+). We use $\binom{e_B e_T}{h_B h_T}$ to describe the spatial location and spin orientation of each charge: e_B

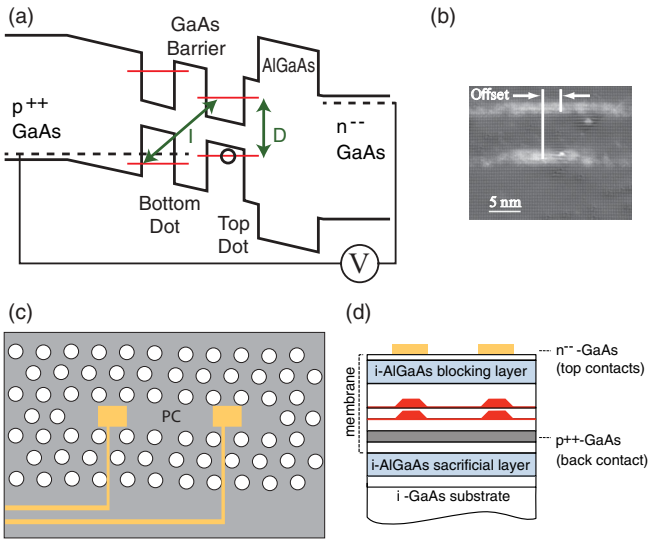

FIG. 1. (Color online) (a) Schematic band diagram of proposed qubit QDM. Direct (D) and Indirect (I) optical transitions are schematically indicated. (b) Cross-sectional STM of a QDM demonstrating the stacking of QDs and the possibility of lateral offsets. (c) Photonic cavity architecture incorporating multiple QDMs. (d) Schematic cross section of device heterostructure.

(e_T) are the electron spin projections in the bottom (top) QD; $\uparrow$, $\downarrow$ correspond to $S_e = \pm 1/2$. Holes in QDs contain both light- and heavy-hole contributions and hole spins are properly described as Luttinger spinors.[30] In single InAs QDs, the heavy-hole-only approximation is largely valid, though the contribution of light holes does impact spin dynamics.[31] In QDMs the contribution of light-hole states becomes more important and leads to unique and tunable properties for hole spins.[32–34] The hole-spin mixing that emerges in QDMs is a key element of the approach we present here.[30,33,35] Although the hole spinors contain contributions from all light- and heavy-hole-spin projections, the spinors are dominated by a single heavy-hole-spin projection. For clarity we label the hole state as $\Uparrow$, $\Downarrow$, corresponding to the dominant heavy-hole-spin projection ($J_z = \pm 3/2$) in each QD. The $\binom{e_B e_T}{h_B h_T}$ notation describes the states of the QDM far away from resonances. When the electric field tunes energy levels into resonance the resulting molecular states can be described as symmetric and antisymmetric combinations of these basis states.

In Figs. 2(a) and 2(b) we plot the calculated energy levels of the h^+ and X^+ states as a function of the applied electric field in the presence of a static 1-T magnetic field applied along the growth axis and optical axis (Faraday geometry). The energy level calculation uses matrix Hamiltonian methods that have been shown to accurately model the states of QDMs.[19–21,32,35–40] The matrix Hamiltonians and numerical values used in the calculations presented here are described in Appendix B. We focus first on the energy levels for the hole (h^+). There are four hole states: $\binom{0,0}{0,\Uparrow}$, $\binom{0,0}{0,\Downarrow}$, $\binom{0,0}{\Uparrow,0}$, $\binom{0,0}{\Downarrow,0}$. We reference energies to the energy of a hole in the top QD, so the two states with a hole in the top QD have an energy that does not depend on electric field [horizontal lines in Fig. 2(b)]. States with a hole in the bottom QD have a linear dependence of energy on the applied electric field [diagonal lines in Fig. 2(b)].

When the hole levels are in resonance, coherent tunneling leads to the formation of molecular orbitals and the appearance of anticrossings, as shown in Fig. 2(b).

The formation of molecular orbitals results in perturbations to the hole-spin g factor and creates the electric-field-dependent Zeeman splitting that can be seen in Fig. 2(b).[20] In the absence of hole-spin mixing, the coherent tunneling that results in molecular orbitals is spin conserving and the four hole states retain their spin values throughout the range of electric field. The presence of a lateral offset between QDs [Fig. 1(b)], however, breaks the QDM symmetry and creates an effective spin-flip-tunneling mechanism that mixes hole states with opposite spin projections located in separate QDs.[35] The magnitude of hole-spin mixing included in these calculations (see Appendix B) does not result in the appearance of anticrossings in Fig. 2(b) because the magnetic field is too small to bring the spin mixed states sufficiently close in energy. The presence of the spin mixing, however, appears in calculations of the hole eigenstate composition. In Fig. 2(c) we plot the relative contribution of each of the four hole basis states to the molecular hole state dominated by $\binom{0,0}{0,\Downarrow}$. Within certain ranges of electric field, the hole-spin mixing leads to eigenstates containing significant contributions from multiple spatial and spin configurations.

We design our qubit and device architecture to take advantage of hole-spin mixing in the optically excited state for initialization and control while suppressing the potential negative consequences of hole-spin mixing in the logical basis states where information is stored. The logical ground states are the spin projections of a single hole confined in a single QD. The use of holes suppresses hyperfine interactions with nuclei and leads to dephasing times estimated to be at least 100 ns for a hole in a single QD.[25] For electric fields to the left of F_P in Fig. 2, the logical basis states approach the electric field of coherent tunneling. The formation of molecular states may have negative consequences for the storage of quantum information, including increased spin-orbit interaction, electric-field-induced changes in g factor, and hole-spin mixing. (We note that all of these effects also provide tools for spin control that may be complementary to the strategy proposed here.) To minimize the potential negative impact of these effects on the storage of quantum information, we design the device architecture to operate only in the range of electric fields to the right of F_P in Fig. 2 where the logical ground states are localized atomic-like states with minimal perturbations of their spin-orbit interaction, g factor, or hole-spin mixing.[30] In Fig. 2(c) we show that the logical basis states remain pure for electric fields to the right of F_P: The molecular state is dominated by $\binom{0,0}{0,\Downarrow}$ with contributions from $\binom{0,0}{\Uparrow,0}$ and $\binom{0,0}{\Downarrow,0}$ below 1% and the contribution of $\binom{0,0}{0,\Uparrow}$ below 0.1%.

The addition of an electron-hole pair to the QDM changes the Coulomb interactions and thus the electric field at which coherent tunneling leads to the formation of molecular states. Our proposed all-optical control strategy operates in the range of electric fields where the logical basis states remain sufficiently pure but the optically excited state can take advantage of hole-spin mixing. As we describe below, hole-spin mixing in the optically excited state allows us to perform all of our spin operations without a transverse magnetic field. Consequently, spin projections along the optical axis are eigenstates of the Hamiltonian and our design is compatible with nondestructive readout. In the next sections we develop the strategy for spin initialization, coherent control, and readout.

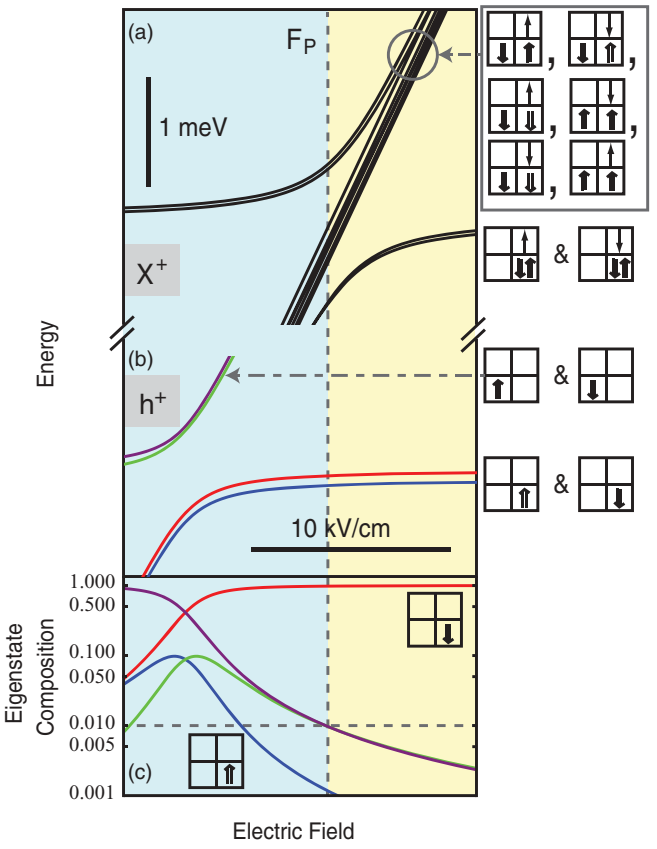

FIG. 2. (Color online) (a) and (b) Calculated energy levels for the X^+ (a) and h^+ (b) states as a function of applied electric field in the presence of a 1-T magnetic field parallel to the optical axis. Right column indicates the dominant atomic-like basis states for each group of molecular states. (c) Hole-spin contributions to one-hole eigenstate as a function of applied electric field.

II. FULL SINGLE-QUBIT OPTICAL CONTROL

We propose to manipulate the qubit states with optical pulses that couple to trion (X^+) states. The X^+ state contains one electron located in the top QD and two holes that can be in either the top or bottom QD. Coulomb interactions with the additional electron and hole cause the anticrossings for the X^+ states to happen in a different range of electric fields than the anticrossings of the h^+ states, as shown in Fig. 2. There are 12 basis states for the X^+ with unique spatial and spin distributions. The two states that have two holes in the bottom QD are outside the energy range we must consider, so only 10 states appear in Fig. 2(a), as described in Appendix A. If both holes are located in the top QD, the Pauli exclusion principle requires them to be in a spin singlet [e.g., $\binom{0,\uparrow}{0,\Uparrow\Downarrow}$)]. If the two holes are in separate QDs, however, both singlet and triplet configurations are possible.[19,21] We denote the singlet state as $\binom{0,\uparrow}{\Downarrow,\Uparrow})_S$ and the three triplet states as $\binom{0,\uparrow}{\Downarrow,\Uparrow})_T$, $\binom{0,\uparrow}{\Uparrow,\Uparrow}$), and $\binom{0,\uparrow}{\Downarrow,\Downarrow}$). An

analogous set of states exist for the electron spin down case (↓).

Coherent coupling of any two states leads to anticrossings of the energy levels. If only spin-conserving tunneling was possible, only the singlet states would tunnel couple [e.g., $\binom{0,\uparrow}{0,\Uparrow\Downarrow} \leftrightarrow \binom{0,\uparrow}{\Downarrow,\Uparrow})_S$] and triplet states would pass through the resonance without coupling. In Sec. IV we show experimental evidence for the existence of hole-spin mixing that couples singlet and triplet states. This hole-spin mixing is included in the calculated energy levels presented in Fig. 2. As a result of this mixing, many of the trion states that appear in Fig. 2(a) are molecular-like admixtures of several basis states. We take advantage of this mixing to enable new optical control strategies.

Figure 4 presents a schematic depiction of the optical transitions used for spin initialization, control, and readout. These optical transitions are "indirect" in that they couple to X^+ states with an electron in the top QD and a hole in the bottom QD. These indirect transitions are responsible for the enhanced wavelength tunability we achieve with this qubit design and control strategy. In Sec. II A we analyze the tunability and optical dipole strength of indirect transitions. In Sec. II B we analyze the spin initialization and readout protocols. We develop the coherent control strategy in Sec. II C.

A. Indirect transitions

Direct transitions, as schematically indicated in Fig. 1(a), involve electrons and holes in the same QDs. These direct transitions [e.g., $\binom{0,\uparrow}{0,\Downarrow}$ and $\binom{0,\downarrow}{0,\Uparrow})$] have a weak dependence of their energy on the applied electric field due to the quantum confined Stark shift. The energy of the direct transition of the neutral exciton (X^0, one electron and one hole) in a QDM with QDs separated by a 4-nm barrier is shown by the black symbols in Fig. 3(a). Indirect transitions, also depicted in Fig. 1(a), involve electrons and holes in separate QDs. Because the relative energy levels of the two QDs shift in response to an applied electric field, indirect transitions [e.g., $\binom{0,\uparrow}{\Downarrow,0}$ and $\binom{0,\downarrow}{\Uparrow,0})$] have a wavelength that depends strongly on the applied electric field. The energy of PL emitted by an indirect X^0 transition is shown by the red symbols in Fig. 3(a). Figure 3(a) demonstrates that the energy of an indirect transition can be tuned by at least 18 meV as the applied electric field is varied from 5 to 45 kV/cm.

The sensitivity of indirect transition energies to applied electric field can be enhanced by placing a thicker barrier between the QDs. However, increasing the thickness of the barrier also decreases the optical dipole matrix element of the indirect transition by reducing the overlap between the wave functions of the electron and hole. To assess the relative strength of the optical dipole matrix element for indirect transitions, in Fig. 3(b) we plot the ratio of PL intensity emitted by indirect and direct transitions. The intensity of PL emission is not a direct measure of the optical dipole strength because the competing dynamics of radiative recombination and carrier relaxation into and between discrete states influences the probability that charges occupy the different optically excited states. For example, when the indirect transition is at higher

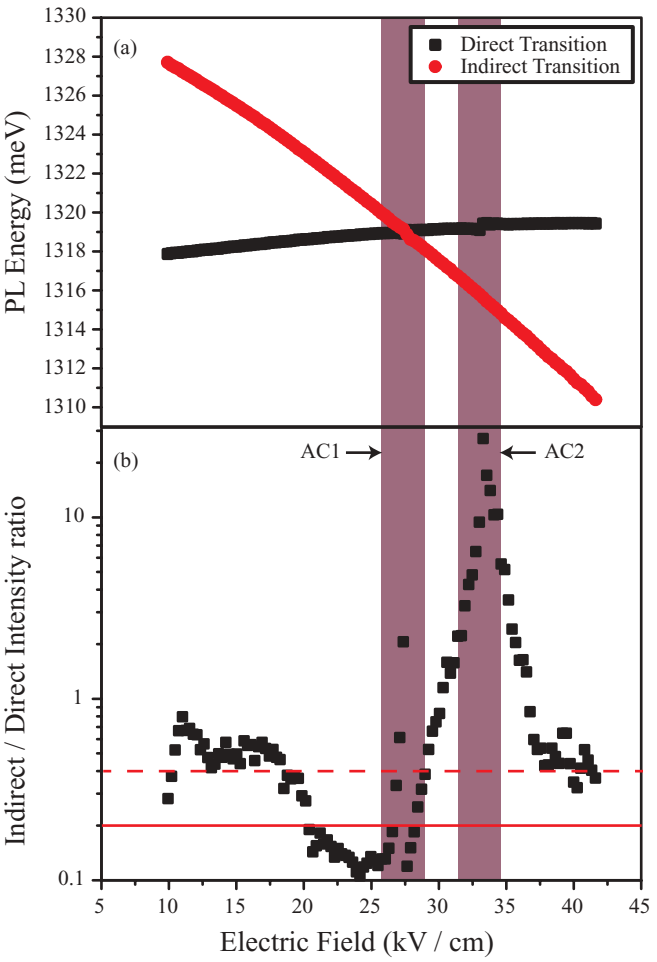

FIG. 3. (Color online) (a) Energy of direct and indirect PL from the neutral exciton in a single QDM as a function of applied electric field. (b) Ratio of PL intensity (indirect/direct) as a function of applied electric field. AC1 indicates the region in which the direct and indirect transitions anticross. AC2 indicates a region in which the energy and intensity of the direct transition is influenced by an anticrossing with an excited indirect transition (not shown).

energy than the direct transition, we would expect that nonradiative relaxation of the hole [e.g., $\binom{0,\uparrow}{\Downarrow,0} \rightarrow \binom{0,\uparrow}{0,\Downarrow})$] would favor emission from the direct exciton and reduce the intensity of the indirect transition. In Fig. 3(b) we observe significant fluctuations in the relative intensity of the PL emitted by indirect and direct transitions. The discontinuity near the anticrossing of the direct and indirect transitions (AC1) is partially due to the fact that the states are fully molecular within this range of electric fields and the distinction between direct and indirect does not apply. The fluctuation in the intensity ratio around AC2 arises because the intensity of the direct transition decreases due to an anticrossing with an excited indirect transition (not shown).

The PL intensity ratio shown in Fig. 3(b) allows us to estimate that the dipole matrix element for indirect transitions in this QDM has an average value approximately 0.4 times the dipole matrix element of the direct transition, as shown by the dashed horizontal line in Fig. 3(b). We note that there can be significant fluctuations between QDMs in the relative intensity of indirect transitions. The particular QDM studied

in Fig. 3 has a somewhat large indirect transition intensity. This increased intensity for the indirect transition is likely correlated to a weak tunnel coupling in this QDM that inhibits hole relaxation between QDs. This conclusion is supported by the observation of a relatively small anticrossing energy. We take 0.2 as a reasonable approximation of the ratio of dipole matrix elements for indirect and direct optical transitions in QDMs with a 4-nm barrier. This value is depicted by the solid red horizontal line in Fig. 3(b) and is used in our device design and QDM modeling. Further investigation of the relationship between QDM structure and the dipole matrix element for indirect transitions can guide engineering of QDMs to enhance the coupling of indirect transitions to optical fields.

B. Initialization and readout

Our spin initialization protocol [Fig. 4(a)] is based on optical shelving. To initialize our qubit in the hole-spin-up state, we illuminate the QDM with σ^- polarized light in resonance with the optical transition that excites from the $\binom{0,0}{0,\Downarrow}$ state to one molecular-like branch of the admixture $\binom{0,\uparrow}{\Downarrow,\Downarrow} \pm \binom{0,\uparrow}{0,\Uparrow\Downarrow}$. This transition is indicated by the 'pump laser' transition in Fig. 4(a). Because the optically excited state $\binom{0,\uparrow}{\Downarrow,\Downarrow}$ is indirect, the energy of this optical transition tunes very strongly with applied electric field, enabling the wavelength tunability we discuss below. The admixture $\binom{0,\uparrow}{\Downarrow,\Downarrow} \pm \binom{0,\uparrow}{0,\Uparrow\Downarrow}$ is possible because hole-spin mixing allows the spin-flip tunneling that couples the hole spin down in the bottom QD with the hole spin-up in the top QD. This mixing, and the consequent formation of a molecular state, is indicated by the $+/-$ joining the two atomic-like basis states. The relative weight of the two basis states does depend on the applied electric field, as we discuss further below.

The optically excited state $\binom{0,\uparrow}{\Downarrow,\Downarrow} \pm \binom{0,\uparrow}{0,\Uparrow\Downarrow}$ may radiatively decay into the $\binom{0,0}{\Downarrow,0}$ state by emission of a direct exciton. $\binom{0,0}{\Downarrow,0}$ is a metastable state in the range of electric fields considered here because the hole in the ground state of the bottom QD is at higher energy than the ground state of the top QD. The hole will thus relax back to the top QD and be again subject to the spin initialization laser. As a result of the hole-spin mixing, there is approximately 1% probability for radiative relaxation from $\binom{0,\uparrow}{\Downarrow,\Downarrow} \pm \binom{0,\uparrow}{0,\Uparrow\Downarrow}$ to the $\binom{0,0}{0,\Uparrow}$ ground state. After such a radiative decay the hole-spin state has been initialized to the spin-up projection. The narrow band pump laser is not resonant with any transitions that couple to the hole-spin-up state, so the hole spin is rapidly shelved in the spin-up projection.

Spin readout is achieved by measuring resonance fluorescence as depicted in Fig. 4(c). The readout states are immune to hole-spin mixing because the Pauli exclusion principle forbids any state with form $\binom{0,\downarrow}{0,\Uparrow\Uparrow}$. The readout states depicted [e.g., $\binom{0,\downarrow}{\Uparrow,\Downarrow})_S$] are in fact molecular states [e.g., $\binom{0,\downarrow}{\Uparrow,\Downarrow})_S \pm \binom{0,\downarrow}{0,\Uparrow\Downarrow})$], but this spin-conserving mixing does not alter the polarization selection rules or enable spin flips of the logical basis states during readout. The direct optical transitions (electron and hole in same QD) of the readout states are strongly suppressed because the parallel projections of electron and hole spin are dark exciton configurations that do not couple to optical fields. The only mechanism for degradation of the readout states is a spin flip of the electron, which can be energetically suppressed by choosing to readout from the lower energy (σ^+) transition. The spin readout transitions are thus cycling transitions compatible with nondestructive readout: many cycles of optical absorption and emission can be undertaken to increase detection probability without risk of altering the spin projection of the logical basis state.[9]

Both the spin initialization and spin readout protocols utilize narrow-band lasers resonant with specific optical transitions. Because the optical transitions used for both initialization and readout are indirect, the energy of this optical transition can be varied with the applied electric field to tune the optical transitions of an arbitrary QDM into resonance with narrow-band initialization and readout lasers utilized for multiple QDMs within the same device. In Fig. 5(a) we plot the energy of optical transitions in the QDM designed for this device strategy. The optical transitions are calculated by taking the difference between the calculated X^+ and h^+ state energies plotted in Fig. 2. We plot results in Fig. 5 only for electric fields above F_P, where the logical basis states remain suitable for all-optical control.

The results plotted in Fig. 5(a) demonstrate that the indirect optical transitions can be tuned by 3 meV (from 1285 to 1288 meV) with applied electric fields ranging between approximately 12 and 20 kV/cm. The linear dependence of wavelength on applied electric field continues far beyond 20 kV/cm, but we restrict Fig. 5 to this range of electric fields for clarity in the discussion of the coherent control protocol.

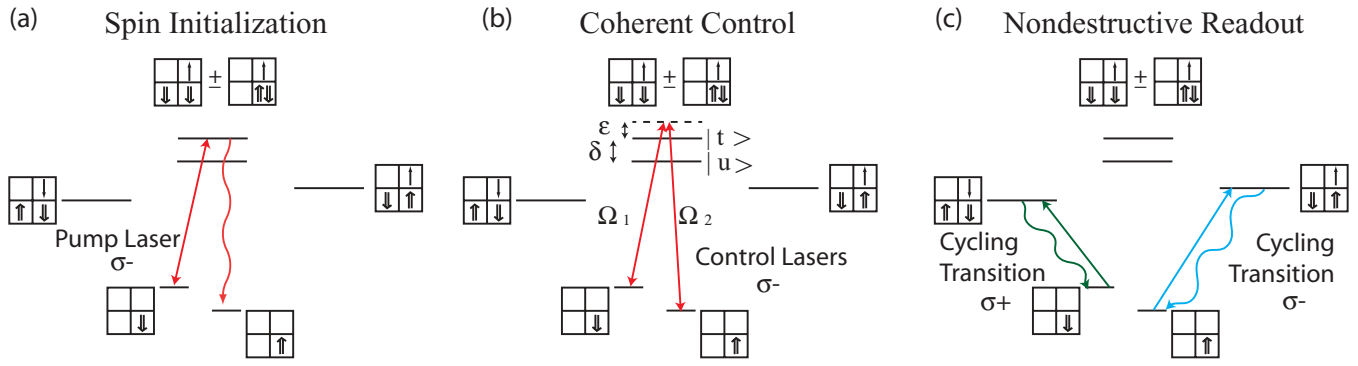

FIG. 4. (Color online) Proposed strategy for (a) spin initialization, (b) manipulation, and (c) readout using optical transitions of QDMs. Top (bottom) rows indicate the spin projections of electrons (holes) in the top (right column) and bottom (left column) QDs.

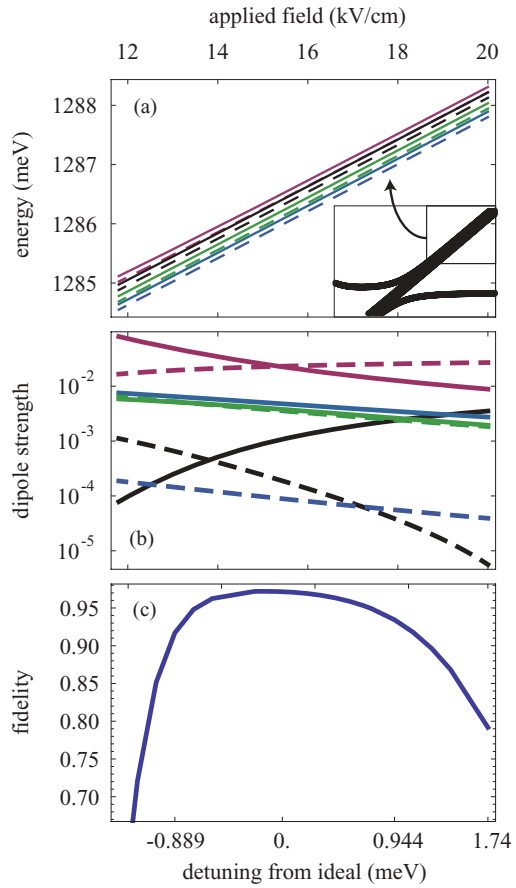

FIG. 5. (Color online) (a) Energies of optical transitions in our designed QDM as a function of applied electric field. The two topmost lines (red) indicate the transitions between the two qubit states and the target X^+ state ($|t\rangle$). The second highest pair of lines (black) indicate the energy of transitions involving the unwanted X^+ state ($|u\rangle$). Other colors indicate the energies of all other transitions with the same polarization (σ^-) that have been included in our calculations. Inset indicates where these transitions lie relative to the anticrossing of the X^+ state. (b) Dipole strengths of each optical transition as a function of applied field. Color and dashing as in top panel. Dipole strengths are measured relative to the dipole for a direct transition, which is given a strength of 1. (c) Calculated fidelity of a $\pi/2$ rotation using the two target transitions in the presence of all parasitic transitions and taking into account dipole variations. The lower axis indicates the QDM's detuning from an ideal laser for each value of the applied electric field.

The maximum wavelength tunability that can be achieved with indirect transitions used for spin initialization and readout will likely be limited by the applied electric field at which the lowest confined hole state of the bottom QD crosses the first excited hole state of the top QD, at which point additional spin interactions and/or relaxation mechanisms could become important. Spectroscopy of the excited states of holes in QDMs suggests that this limit would permit tuning over approximately 10 meV.[40]

Tuning over 10 meV is an order of magnitude improvement over the typical Stark shift tuning (of order 1 meV) achieved for single InAs QDs[14] and comparable to the giant Stark shift that can be achieved for single QDs confined between AlGaAs barriers.[41] In our QDM design the AlGaAs layer that blocks injection of carriers from the n-type GaAs can be moved arbitrarily far away from the QDs. As a result, our QDM design is likely to be more compatible with the fabrication of photonic crystal cavities than single QDs that achieve a giant Stark shift by placing AlGaAs layers in close proximity to the QDs. As discussed in Sec. II A, the dipole matrix element for indirect transitions is weaker than the comparable dipole matrix element for a direct transition. We discuss the impact of these dipole matrix elements in more detail below.

C. Spin rotations

In this section we develop our approach to the implementation of single-qubit rotations. We quantify the quality of our gates by calculating the fidelities of our spin rotations in the presence of loss mechanisms and unwanted dynamics.

To implement arbitrary spin rotations we must be able to perform rotations about two orthogonal axes; rotations about other axes can be implemented by combining those. In our present proposed design, rotations about the quantization (z) axis will be carried out using the cycling (measurement) transitions: A cyclic pulse on the σ^- measurement transition will induce a phase and implement a rotation about the z axis by an angle determined by the detuning.[4,5] The detuning can be controlled independently for each qubit state (defined by an individual QDM) using the electric field that tunes the indirect transition relative to a fixed optical source frequency. Coherently exciting the two target (Raman) transitions along the quantization axis with circularly polarized light allows us to implement rotations about an orthogonal axis.

To implement rotations about the x axis we propose the use of the Λ system formed by the two qubit states $[\binom{0,0}{0,\Downarrow}$ and $\binom{0,0}{0,\Uparrow}]$ and one of the spin-mixed trion states, as depicted in Fig. 4(b). As shown in Fig. 4(b), there are two excited states [the spin-mixed trion states $\alpha_\pm\binom{0,\uparrow}{\Downarrow,\Downarrow} \pm \beta_\pm\binom{0,\uparrow}{0,\Uparrow\Downarrow}$] that are very close in energy. We develop our strategy based on the use of the high-energy spin-mixed trion state for the Raman transition and label this state $|t\rangle$, for target. We want to avoid the low-energy spin-mixed trion state and label this state $|u\rangle$, for unwanted. We will return to the impact of this unwanted state below.

The two atomic-like basis states that contribute to the spin-mixed molecular state $|t\rangle$ involve direct and indirect transitions with significantly different optical dipoles. A key advantage of our scheme is that the molecular state that mediates the Raman transition is dominated by the triplet state that is excited by the indirect transition $[\binom{0,\uparrow}{\Downarrow,\Downarrow}]$. Hole-spin mixing adds a small fraction of the singlet state excited by the direct transition $[\binom{0,\uparrow}{0,\Uparrow\Downarrow}]$. Because the molecular state is dominated by the triplet configuration basis state, the dipole matrix element for the indirect transition is comparable to the direct transition. Both transitions have the same polarization. The energy levels and dipole strengths are computed assuming a hole-spin-mixing strength of 300 μeV, which we believe to be a value achievable with present growth methods (see Sec. V and Appendix B).

Spin rotations about the x axis are based on coherent population trapping (CPT). As developed in Ref. 5 we can create an effective two-level system by using two appropriate phase-locked pulses, each focused on one of the legs of the

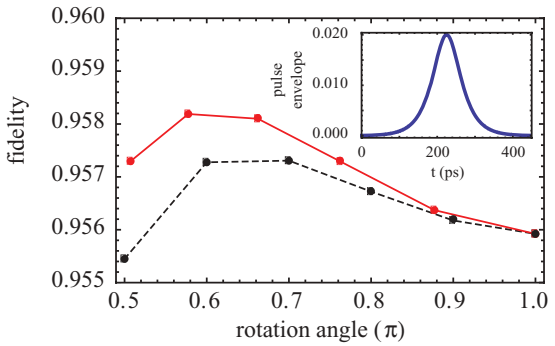

FIG. 6. Fidelity as function of angle of rotation for 'traditional' approach (dashed black line) in which the laser is detuned and our new approach (solid red line) in which the QDM is tuned relative to a fixed laser. The π-rotation is implemented by a resonant set of pulses, in which case the two approaches coincide. Inset: temporal profile of the hyperbolic secant pulses used in our simulations (intensity in a.u.). The bandwidth of the pulse is 0.02 meV; the optical decay time is taken to be 1ns.

Λ system. We create an effective two-level system when the parameters of the two pulses are related in a certain way;[5] physically, a dark state is created. When the two transitions have the same Rabi frequency, the bright state is an equal superposition of $\binom{0,0}{0,\Downarrow}$ and $\binom{0,0}{0,\Uparrow}$. Therefore a cyclic evolution will induce a phase to this superposition state and implement a rotation about the x axis. The angle of rotation can be controlled by the detuning [ε in Fig. 4(b)], which is the same for both legs.

There are always sources of error that will lower the fidelity of the spin rotations. The finite lifetime of the excited state will introduce nonunitary evolution and therefore will reduce the purity of the qubit. The unwanted state $|u\rangle$, along with other parasitic transitions, will alter the unitary dynamics and lower the quality of the gate. Finally, there is an additional error coming from the fact that the pulse that is meant to excite one transition of the Λ system will also affect the other one. This is because the two transitions have the same polarization. To quantify the effects of these error mechanisms and compare our approach to the "traditional" approach in which the control lasers are tuned relative to the fixed frequency of QD optical transitions, we calculate the fidelity of the gate. The fidelity is calculated as $\langle \mathrm{Tr}(\rho_t \rho)\rangle_\Psi$, where ρ_t is the density matrix corresponding to the target final state when starting from initial state Ψ, ρ is the actual final density matrix, and the average is taken over all initial spin states. The fidelity for the "traditional" approach is plotted by the dashed black line in Fig. 6 as a function of the angle of the x rotation. The angle of rotation is controlled by varying the detuning of the laser while the electric field applied to the QDM, and thus the optical transition energies of the QDM, remain fixed. We choose a fixed electric field of 15.3 kV/cm, where the dipole strengths of the two branches of the Raman transition are equal [see Fig. 5(b)]. The inset to Fig. 6 shows the temporal pulse envelope used in these calculations. In the next section we assess the impact of changing dipole strengths and electric fields on the fidelity of tunable spin rotations implemented using our approach.

D. Tuning spin rotations for a single QDM

As discussed above, the angle of coherent spin rotations can be controlled by varying the detuning of the lasers relative to the optical transitions [ε in Fig. 4(b)]. In traditional device designs the laser would be tuned relative to the fixed frequency of optical transitions of the QD or QDM that defined the qubit. The fidelity of gate operations that can be achieved for our QDMs using the traditional approach is plotted by the dashed black line in Fig. 6. Our design achieves improved scalability by utilizing laser sources with fixed frequency and tuning individual qubits into resonance with the available sources. The tunability can be used both to select which qubits are affected by the lasers and to control the detuning in order to control the angle of rotation. Unfortunately, the applied electric field that tunes the energies also changes the dipoles of the transitions because the composition of the states varies. As a result, the dipoles do not remain constant when we vary the applied electric field in order to control the detuning. These varying dipoles are shown in Fig. 5(b).

To show that the variation in dipole matrix elements does not prohibit execution of spin rotations by arbitrary angles, we calculate the fidelity for spin rotations executed by tuning QDMs relative to a fixed frequency laser source. The computed fidelities are shown by the solid red line in Fig. 6. The calculations include all sources of error considered for the traditional approach in addition to the changing dipole strengths. The laser pulse profile and frequency remain constant and the angle of rotation is varied by tuning the electric field to control the detuning (ε). The plotted value indicates the best fidelity that can be achieved for a given angle of rotation using the design from Ref. 5 without additional pulse shaping. To compensate for the unequal dipoles we vary the relative intensity of the two lasers that address the two legs of the Λ transition. Rapid modulation of laser power for each target rotation will be challenging, but should be achievable with electro-optic modulators. The optical decay time is taken to be constant at 1 ns because direct radiative recombination will likely remain the dominant lifetime limit. Figure 6 shows that the fidelity of gate operations implemented with our approach is, in fact, slightly better than that achieved by the traditional approach. The electric field must be tuned by only 0.05 kV/cm to affect the change from a $\pi/2$ to a π rotation. Figure 6 uses simple pulse shapes and therefore provides a conservative estimate of the fidelities that can be achieved with our approach.

III. SCALABILITY

In this section we address two important aspects of scalability. First, we examine the tunability of the system, in the sense of fixing a modest number of optical sources and tuning the QDMs into resonance with those sources. This approach allows for a substantial decrease in the equipment overhead and device complexity. Second, we develop an approach for coupling arbitrary pairs of qubits without increasing our laser overhead.

A. Tunability in a multi-QDM system

In the ideal case, all QD-based qubits would be identical and could be addressed by a single group of optical sources. In

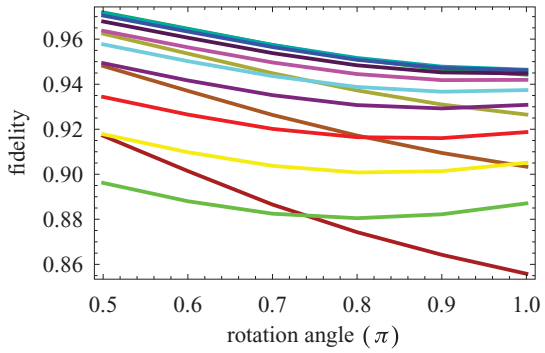

FIG. 7. (Color online) Fidelity of spin rotation as a function of the angle of rotation for a multi-QDM system with variations in their optical resonances. Each curve corresponds to a different value of the E field; from top to bottom at $\phi = \pi/2$: 13.8, 14.7, 15.3, 15.6, 16, 16.4, 16.8, 17.2, 13.4, 17.7, 18.1, 19.3 kV/cm. The pulse envelope is similar to that used in Fig. 6 but with half the bandwidth, so about double in temporal length.

reality, the inhomogeneous distribution of energy levels in QDs makes this impossible. A mechanism for tuning the optical initialization, control, and readout transitions into resonance with a small number of fixed-frequency optical sources is therefore desirable for the development of a realistic, scalable, multiqubit device. We have analyzed the wavelength tunability of the spin initialization and readout transitions above, and addressed spin rotation tunability within a single qubit. We now address the wavelength tunability of our spin rotations in the case of a system of inhomogeneous QDMs.

The inhomogeneous distribution of QD energy levels means that an arbitrary QDM qubit will not have equal dipoles for the two legs of the Λ transitions when that QDM qubit is tuned into resonance with the laser sources. As a result, Fig. 6 is not general enough to describe a multi-QDM system. To analyze the multi-QDM system we compute the fidelity versus rotation angle for various values of the E field, which simulates the need to tune an individual QDM farther away from the ideal electric field (at which the dipole strengths of the two transitions are equal) in order to tune that QDM into resonance with the available optical source. The results are plotted in Fig. 7. The different lines correspond to different applied electric fields with the consequent different relative dipole strengths for the Λ transition. In this calculation we do not correlate the detuning of the target transitions to the dipoles. Figure 7 therefore describes the range of fidelities that could be achieved for a QDM ensemble with a certain energy distribution.

To further quantify the range of tuning that could be achieved for an arbitrary QDM qubit, we plot the fidelity for a $\pi/2$ rotation as a function of electric field applied to tune the QDM into resonance with a fixed laser source. The results, presented in Fig. 5(c), show that our scheme can achieve a fidelity of at least 0.8 when tuning a particular QDM to use a fixed-frequency laser anywhere within a 5-meV window. A fidelity of 0.8 is certainly well below the formidable values ($\sim$99.99%) needed for practical quantum computation. The present fidelity values are intended to illustrate that it is feasible to tune individual QDMs to utilize fixed-frequency laser sources and should be viewed as a lower bound of what can be achieved. The present calculations have used very simple pulse shapes and there are ways to increase the fidelity of the operations by using numerical pulse optimization techniques to design pulse shapes tailored to this system. In particular, by the use of optimal control theory we can impose the condition that the rotation is robust against substantial variations in the ratio of the dipole couplings. This could be done by running a Krotov algorithm in parallel for a number of systems with varying dipoles. Similar approaches can improve fidelities against other types of errors, such as unintended couplings to other states. We expect that with such techniques the fidelities should approach the near-perfect values needed for realistic quantum information processing.

B. Two-qubit gates

The wavelength tunability enabled by our QDM-based qubit design provides a unique opportunity to couple arbitrary pairs of qubits through a photonic crystal cavity mode. As depicted in Figs. 1(c) and 1(d), the qubits in our proposed device architecture are defined by QDMs that are deterministically spatially coupled to a single photonic crystal membrane cavity mode.[42] The wavelength of the photonic crystal mode can be fine tuned,[43] but the QD inhomogeneity makes it extremely challenging to choose a cavity resonance that is ideal for all qubits if they are defined by as-grown QDs or QDMs. Our QDM qubit design allows each QDM to be individually controlled by local electric field gates to provide *in situ* tuning of the coupling between individual QDMs and the cavity mode. We propose to use p- and n-type GaAs as the electrical contacts in order to avoid the inclusion of metals, which would heavily degrade the cavity quality factor.[44] During device calibration, the local electric field necessary to tune each QDM into resonance with the available optical sources and/or cavity mode would be determined. During the execution of logic operations, each QDM can be tuned appropriately with respect to these optical sources and the cavity. (We note that conventional photonic cavity designs support linear polarization modes, but circularly polarized modes are advantageous for spin control. Because the cavity is off-resonant from the (narrowband) laser sources, their direct interaction is very weak. The lasers rather interact directly with the QDMs. Therefore, we do not expect the laser polarization to be affected by the cavity.)

Using the approach of Ref. 45, pairwise entanglement can be created via cavity-mediated entangling gates by selectively tuning two QDMs to the appropriate detuning relative to the cavity mode. The remaining qubits are isolated by significantly detuning them relative to the cavity via use of their local electric fields. The cavity-mediated entanglement, described in more detail below, occurs only when a laser pulse is present, suppressing the possibility of unintended couplings as the QDMs are tuned in preparation for each logical gate operation. The optical transitions relevant to coherent single-spin rotations, readout, and two-qubit gates are all among the highest-energy transitions shown in Fig. 5(a). Consequently, the QDMs can be red-detuned relative to the cavity when they are to be isolated, ensuring that other optical transitions of the QDM never become more strongly coupled to the cavity mode.

Our proposed cavity-mediated two-qubit gates are based on the readout transitions $\binom{0,0}{0,\Uparrow} \leftrightarrow \binom{0,\downarrow}{\Uparrow,\Downarrow}_S \pm \binom{0,\downarrow}{0,\Uparrow\Downarrow}$. Bringing these

transitions near the two-photon resonance with the cavity,[45] we can diagonalize the Hamiltonian consisting of one qubit state and the direct trion excited by a fixed circular polarization for each of two QDMs and by three photonic number states: the zero-, one-, and two-photon states. The eigenstates of this Hamiltonian will be entangled states of all three systems (QDM1, QDM2, photon), and will naturally separate into subspaces, depending on the number of excitations.[45] These eigenstates have energies that are shifted from the sum of the noninteracting system's net energy, and thus a specific entangled state can be selectively excited optically. The requirement on the cavity is that its Q is high enough that its line broadening is smaller than the Zeeman energy of the qubits and that the QD-cavity coupling g is larger than the decay rates involved. These requirements ensure that the other qubit states will not couple to the cavity and each other and that two-qubit unitary operations are in principle possible. Under these conditions, we can use a single cyclic pulse to induce a π phase on the state $|\Uparrow_1\Uparrow_2\rangle$, by which we mean the state of two qubits, each in their own QDM, both with hole spin-up. Inducing a π phase on the state $|\Uparrow_1\Uparrow_2\rangle$ effects an entangling CZ gate.[45]

IV. EXPERIMENTAL EVIDENCE OF HOLE-SPIN MIXING IN OPTICALLY EXCITED STATES OF QDMS

As a first step toward implementing this device architecture, we experimentally measure the magnitude of hole-spin mixing in the positive trion (X^+) state. The QDM studied experimentally has a 4-nm barrier separating the two QDs, identical to the barrier in the QDM proposed here. The QDM we measured is grown on an n-type substrate and is optically (not electrically) charged with a single excess hole.[19,20] The built-in electric field and QD asymmetry of this sample are also inverted relative to the sample described above. None of these changes impact the spin mixing interactions that are the focus of this experiment. The sample is prepared with an ohmic back contact and Schottky top contacts enabling us to study individual QDMs using photoluminescence (PL) spectroscopy as a function of both applied electric and magnetic fields. A detailed description of experimental procedures can be found in previous publications.[33] Here we present the evidence of hole-spin mixing in the optically excited trion states (X^+), which manifests as new anticrossings in the photoluminescence (PL) spectra. We compare computational simulations of the observed PL spectra to extract a numerical value of the hole-spin mixing strength.

In Fig. 8(b) we show the experimentally measured PL spectra of a single QDM in the presence of a 6-T magnetic field. The figure plots the photoluminescence intensity (grayscale) as a function of both applied electric field (x axis) and energy (y axis). The initial and final states of optical recombination are the X^+ and h^+ states, analogous to those displayed in Figs. 2(a) and 2(b). As seen in Fig. 2, Coulomb interactions cause the anticrossings of the X^+ and h^+ states to occur at different values of the applied electric field. As a result, the PL energy as a function of electric field shows the characteristic "x" shaped pattern.[19] Note that the "x" appears doubled because the magnetic field introduces a Zeeman splitting between states that have a total flip of all spins. The circled regions indicate the locations of anticrossings and fine structure that arise due to hole-spin mixing.

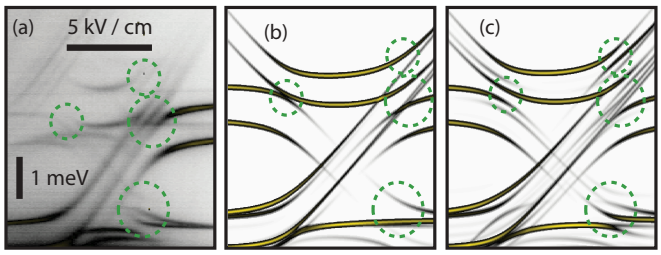

FIG. 8. (Color online) Experimental and calculated spectra from the positive trion in a QDM with a 4-nm barrier in a 6-T longitudinal magnetic field. (a) Experimental spectra, (b) calculation with $hm = 0$, (c) calculation with $hm = 0.2$ meV. The circles highlight four regions where the features observed experimentally are only reproduced by the calculation including nonzero hm.

In Figs. 8(b) and 8(c) we show calculated PL spectra computed with the matrix Hamiltonian method described in Appendix A and in previous publications.[33] In Fig. 8(b) the hole-spin mixing term (hm) is set to zero and in Fig. 8(c) the hole-spin mixing term is set to 0.2 meV. It is clear that the inclusion of the hole-spin mixing term generates the additional anticrossings and fine structure apparent in the circled regions. The value of $hm \sim 0.2$ meV is obtained by varying the magnitude of hm and evaluating the best fit to the experimental data. This result experimentally verifies the existence of hole-spin mixing in the trion state and validates the feasibility of the qubit design and device architecture proposed here.

V. CONTROLLABLY GENERATING HOLE-SPIN MIXING WITH THE DESIRED MAGNITUDE

For the qubit and device designs we propose, strong spin mixing is desirable because it separates the target ($|t\rangle$) and unwanted ($|u\rangle$) states. The energy level calculations presented in Fig. 2 use a value of $hm = 0.3$ meV, and the energy levels and dipole matrix elements computed with these parameters are the basis for the calculated fidelity presented in Fig. 5(c). The fidelity results would improve for larger values of hm.

As discussed in Ref. 35, holes are described as Luttinger spinors with coupled heavy hole (HH) and light hole (LH) components. The hole pseudospin projections in self-assembled QDs, $\Uparrow$ and $\Downarrow$, can be identified with the total angular momentum of the Luttinger spinors, $F_z = 3/2$ and $F_z = -3/2$. When the axial symmetry of the nanostructure is broken, F_z is no longer a good quantum number and hole-spin mixing (i.e., coupling between $F_z = 3/2$ and $F_z = -3/2$ states) arises. The admixing of the two pseudospins is mediated by the LH components of the spinor.[35] In QDMs, the constituent QDs are usually symmetric enough to neglect this spin mixing mechanism. If the QDM is misaligned, however, the application of an electric field forcing the hole to delocalize over the two QDs leads to a severely asymmetric orbital and spin mixing becomes important. In Fig. 1(b) we show a cross-sectional STM of stacked InAs QDs that shows the possibility of symmetry breaking due to lateral offset along the stacking axis. Clearly, the larger the lateral offset between

the QDs of the QDM, the stronger the asymmetry and the stronger the spin mixing. Using k·p calculations we previously showed that a QDM could give rise to $hm = 0.1$ meV for center-to-center lateral offsets of ~ 5 nm.[35] A 5-nm offset is unusually large but within the observed range.[35]

As described in Sec. IV, we have now experimentally measured values of hm up to ~ 0.2 meV. In order to further increase hm one could use larger offsets, but this structural parameter is unfortunately difficult to control. Moreover, increasing the offset has the negative side effect of reducing the tunneling rate.[35] In this section we propose a more efficient way to enhance the spin mixing by using QDs with larger aspect ratio (i.e., larger ratio of height to radius). Larger aspect ratios qualitatively increase the hole-spin mixing because the anisotropic masses of HHs and LHs cause the LH character to increase with increasing aspect ratio in QDs grown along the [001] (z) direction. As a result of the increased LH character the pseudospin coupling increases. We analyze the strength of hole-spin mixing as a function of QDM structure using k·p theory and demonstrate that this approach provides a feasible path to fabrication of QDMs with $hm \geqslant 0.3$ meV.

The spin mixing parameter hm is defined as the matrix element coupling states with holes localized in opposite QDs and with opposite spin. We analyze the dependence of this spin mixing parameter on QDM structure and symmetry with a simplified Hamiltonian. In a basis formed by $|a\rangle = \binom{0,0}{\Uparrow,0}$ and $|b\rangle = \binom{0,0}{0,\Downarrow}$, the spin mixing Hamiltonian reads

$$\begin{pmatrix} E_a + ed\,F & hm \\ hm & E_b \end{pmatrix}, \tag{1}$$

where E_a and E_b are the energies of $|a\rangle$ and $|b\rangle$ at zero electric field. At the resonant electric field $(E_a + edF) = E_b = E_0$ and the two hybridized states have energies $E_\pm = E_0 \pm hm$. Thus, $hm = \Delta/2$, where $\Delta = E_+ - E_-$ is the magnitude of the spin anticrossing gap between $\binom{0,0}{\Uparrow,0}$ and $\binom{0,0}{0,\Downarrow}$.

To determine Δ, we run numerical simulations using the same theoretical model and material parameters as in Ref. 35. A typical hole energy spectrum as a function of the external electric field is presented in Fig. 9(a) . The spectrum is calculated with a magnetic field $B = 6$ T to separate the spin-conserving anticrossings ($F \sim -2$ kV/cm) from the spin anticrossings we are interested in ($F \sim 0$ and $F \sim -4$ kV/cm; see arrows). We note that in our formulation of the k·p Hamiltonian there are no off-diagonal magnetic terms, so the strength of the HH-LH coupling terms does not depend on B.[46]

Figure 9(a) reveals that there are two spin anticrossings, Δ_0 and Δ_1. In general the magnitude of the anticrossings is asymmetric, with $\Delta_0 > \Delta_1$. This is because the spin mixing is mediated by LHs delocalized over the entire QDM. HHs come into resonance at $F \sim -2$ kV/cm, but LH states come into resonance at electric fields closer to 0 kV/cm because of their lighter vertical mass. Consequently, the Δ_0 anticrossing is closer to the resonant field of LHs, where LH delocalization and hence spin mixing are maximized.

In Fig. 9(b) we plot the magnitude of Δ_0 for different QDMs as a function of the lateral offset. The QDMs are made of lens-shaped QDs with $H = 2$ nm height, radius R, and interdot barrier D. Because we are interested in strong spin mixing, we focus on large (but experimentally accessible) offsets. For QDs with $R = 15$ nm, Δ_0 reaches maximum values of 0.2 meV ($hm = 0.1$ meV), which is the case reported in Ref. 35. For QDs with $R = 13$ nm Δ_0 is systematically larger, and $hm = 0.15$ meV is attained for a 5-nm offset. Last, for QDs with $R = 10$ nm the magnitude of the spin mixing is even stronger and $\Delta_0 = 0.6$ meV ($hm = 0.3$ meV) is already within reach.

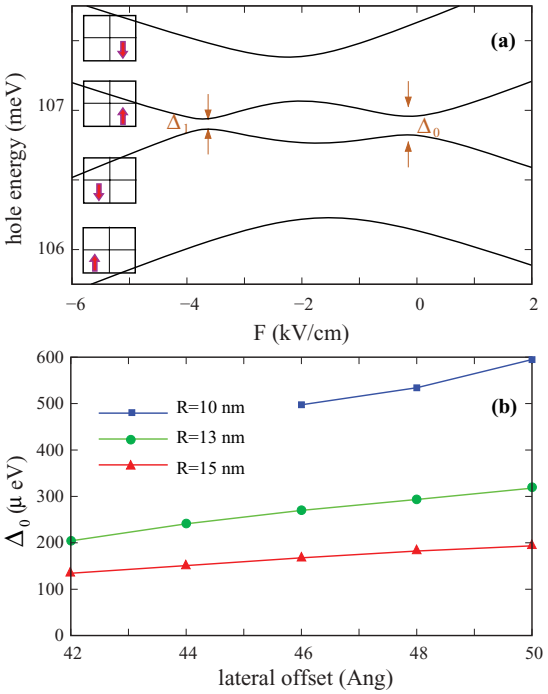

FIG. 9. (Color online) (a) Single hole energy as a function of the electric field in a QDM subject to $B = 6$ T. The QDs have $H = 2$ nm, $R = 15$ nm, $D = 1.8$ nm, and are offset by 4.2 nm. (b) Spin anticrossing gap as a function of the QDM offset for QDs with different aspect ratio. Triangles correspond to $(R, D) = (15, 1.8)$ nm, circles to $(R, D) = (13, 1.7)$ nm, and squares to $(R, D) = (10, 1.6)$ nm.

Similar trends to those reported in Fig. 9(b) are obtained for Δ_1, albeit with smaller magnitude ($\Delta_1 \lesssim \Delta_0/2$). One could think of increasing the QD aspect ratio by growing taller QDs instead of reducing R. However, this also reduces the tunneling rate of the QDM, so reducing the lateral size is preferable. The lateral size of InAs QDs can be controlled experimentally by growing on templated surfaces.[47] It may also be possible to use new methods for the growth of QDMs with precisely tailored three-dimensional configurations to engineer physical interactions that maximize wavelength tunability and gate operation fidelity.[48]

VI. SUMMARY

We have presented a scalable qubit design and device architecture based on the spin states of single holes confined in a QDM. The QDM qubit enables a new strategy for all-optical coherent control via indirect optical transitions. The wavelength tunability of indirect transitions allows us to develop a device architecture in which locally applied electric fields are used to tune individual QDMs into resonance with a single photonic cavity mode or a small number of

optical sources at fixed wavelengths. Thus, our design offers a tremendous reduction in the required overhead as compared to schemes based on single QDs. We take advantage of hole-spin mixing in order to execute spin initialization and coherent spin rotations with indirect optical transitions and without transverse magnetic fields. The absence of transverse magnetic fields enables nondestructive readout. We show how cycling transitions can be used for nondestructive readout by optically exciting trion states that are immune to hole-spin mixing. We demonstrate that ultrafast coherent spin rotations can be achieved by tuning the indirect transitions of individual QDMs into resonance with a single optical pulse or a pair of pulses. We show that these spin rotations have a minimum fidelity of 0.8 over a minimum tuning range of 2.5 meV, despite fluctuating dipole strengths, and describe a path to the development of optical control protocols that can enhance the fidelity and the wavelength tunability of this approach. We demonstrate experimental and theoretical progress toward the development of QDM materials to implement the designs presented and validated here.

ACKNOWLEDGMENTS

S.E.E. acknowledges support from the Laboratory for Physical Sciences–National Security Agency (NSA) and in part from the Office of Naval Research. A.S.B. and D.G. acknowledge support from Army Research Office–NSA. J.I.C. acknowledges support from MICINN Project No. CTQ2011-27324. M.F.D. acknowledges support from the National Science Foundation award Grant No. ECCS-1101754.

APPENDIX A: QDM DESIGN PARAMETERS

The substrate doping, choice of QD asymmetry and applied electric field can be used to control the total charge occupancy and spatial location of charges in a QDM.[29] The qubit we present here is designed to induce controlled coupling of hole energy levels in a range of electric fields in which the QDM remains charged with only one hole. The thickness of the undoped GaAs separating the QDs from the p-doped region (25 nm) is set by the Coulomb blockade strength and allows for deterministic charging of the QDM with a single hole. The QD asymmetry (bottom QD truncated to 2.8 nm, top QD truncated to 3.2 nm) is chosen to ensure that hole levels come into resonance for the sign and range of electric fields applied in the p-i-n diode structure. This asymmetry and sign of the applied electric field also ensure that the electron is located in the top QD.

The thickness of the GaAs separating the top QD from the AlGaAs blocking layer is less critical; it is only necessary to ensure that that the AlGaAs layer is sufficiently thick to suppress tunneling of electrons from the n-doped GaAs top contact and sufficiently far away from the QD to avoid altering growth dynamics or hole confinement. Because the thickness of the GaAs and AlGaAs layers above the top QD are flexible, the net thickness of the heterostructure can be chosen to provide the optical confinement necessary to fabricate a high-Q photonic crystal that places the QDMs at electric field maxima. The $Al_xGa_{(1-x)}As$ ($x \geqslant 0.7$) sacrificial layer is included below the p-doped GaAs region in order to facilitate an undercut etch that releases the photonic crystal membrane.

APPENDIX B: COMPUTATIONAL MODEL

The energy levels, optical transitions, and optical dipoles presented above are calculated using matrix Hamiltonian methods presented in previous publications.[19–21,32,35–40] The relevant basis states for the optical ground state (logical basis states) are

$$\begin{pmatrix} 0 & 0 \\ 0 & \Uparrow \end{pmatrix}\begin{pmatrix} 0 & 0 \\ 0 & \Downarrow \end{pmatrix}\begin{pmatrix} 0 & 0 \\ \Uparrow & 0 \end{pmatrix}\begin{pmatrix} 0 & 0 \\ \Downarrow & 0 \end{pmatrix}. \tag{B1}$$

In this basis, the matrix Hamiltonian that describes the hole states is given by

$$\begin{pmatrix} \frac{1}{2}\mu_B B g_h & 0 & -t_h + \frac{1}{2}\mu_B B g_b & -hm \\ 0 & -\frac{1}{2}\mu_B B g_h & hm & -t_h - \frac{1}{2}\mu_B B g_b \\ -t_h + \frac{1}{2}\mu_B B g_b & hm & dF + \frac{1}{2}\mu_B B g_h & 0 \\ -hm & -t_h - \frac{1}{2}\mu_B B g_b & 0 & dF - \frac{1}{2}\mu_B B g_h \end{pmatrix}. \tag{B2}$$

The definitions and numerical values for each symbol are provided in Table I. The basis states for the positive trion (X^+) matrix Hamiltonian are

$$\begin{pmatrix} 0 & \uparrow \\ 0 & \Uparrow\Downarrow \end{pmatrix}\begin{pmatrix} 0 & \uparrow \\ \Uparrow & \Downarrow \end{pmatrix}_S\begin{pmatrix} 0 & \uparrow \\ \Uparrow & \Downarrow \end{pmatrix}_T\begin{pmatrix} 0 & \uparrow \\ \Downarrow & \Downarrow \end{pmatrix}\begin{pmatrix} 0 & \uparrow \\ \Uparrow & \Uparrow \end{pmatrix}, \tag{B3}$$

TABLE I. Definitions and numerical values for computational parameters.

E_{X^+}	1280 meV	Energy of the trion
$-t_h$	−0.3 meV	Bare hole tunneling strength
$-t_{X^+}$	−0.45 meV	Hole tunneling strength in trion state
d	4 nm	QD separation
F	Varies	Applied electric field
hm	0.3 meV	Hole-spin mixing strength
μ_B	57.9 μeV/T	Bohr magneton
B	1 T	Magnetic field
g_h	−1.555	Hole g factor
g_b	0.4	Barrier contribution to hole g factor
g_e	−0.64	Electron g factor
Γ	3.2145 meV	Energy shift due to Coulomb interactions when all three charges are in the same QD
J	0.116 meV	Electron-hole exchange energy

In this basis, the matrix Hamiltonian that describes the positive trion state is given by

$$E_{X^+} = \begin{pmatrix} \Gamma - \frac{1}{2}\mu_B B g_e & -t_{X^+} & 0 & hm & hm \\ -t_{X^+} & dF - \frac{1}{2}\mu_B B g_e & J & 0 & 0 \\ 0 & J & dF - \frac{1}{2}\mu_B B g_e & 0 & 0 \\ hm & 0 & 0 & dF + J - \frac{1}{2}\mu_B B\,(g_e + 2g_h) & 0 \\ hm & 0 & 0 & 0 & dF - J - \frac{1}{2}\mu_B B\,(g_e - 2g_h) \end{pmatrix}. \tag{B4}$$

Note that the full matrix is block diagonal with a submatrix for the electron spin $-1/2$ that exactly parallels the $+1/2$ case presented here. The parameter definitions and numerical values are given in Table I.

The energies of hole and trion states are computed by calculating the eigenvalues of the matrix Hamiltonian as a function of electric field, F. The hole-spin purity [Fig. 2(c)] is calculated by plotting the relative contributions of each basis state to the eigenvector that describes the admixture of all states for a given value of F. The dipole matrix elements are computed by the product $\Psi_h \cdot \hat{S} \cdot \Psi_{X^+}$ where Ψ_h and Ψ_{X^+} are the eigenvectors describing the hole and trion states at a given value of F. $\hat{S}$ is a matrix describing the selection rules for all optical transitions. $\hat{S}$ assigns amplitude 1 to all bright direct transitions (i.e., electron and hole in the same QD with opposite spin projections), amplitude 0 to all dark transitions, and amplitude $\frac{1}{2}$ to all transitions involving singlets or triplets that are superpositions of a bright and a dark direct transition. Bright indirect transitions in $\hat{S}$ are given amplitude 0.2, consistent with the measured ratio of optical intensities for direct and indirect transitions in samples where the QDs are separated by a 4-nm barrier. Indirect transitions that involve singlets or triplets that are superpositions of a bright and a dark state are given amplitude 0.1.

*doty@udel.edu

[1] A. Imamoglu, D. D. Awschalom, G. Burkard, D. P. DiVincenzo, D. Loss, M. S. Sherwin, and A. Small, Phys. Rev. Lett. **83**, 4204 (1999).

[2] X. Li, Y. Wu, D. Steel, D. Gammon, T. H. Stievater, D. S. Katzer, D. Park, C. Piermarocchi, and L. J. Sham, Science **301**, 809 (2003).

[3] P. C. Chen, C. Piermarocchi, L. J. Sham, D. Gammon, and D. G. Steel, Phys. Rev. B **69**, 75320 (2004).

[4] S. E. Economou, L. Sham, Y. Wu, and D. Steel, Phys. Rev. B **74**, 205415 (2006).

[5] S. E. Economou and T. L. Reinecke, Phys. Rev. Lett. **99**, 217401 (2007).

[6] M. Atatüre, J. Dreiser, A. Badolato, A. Hogele, K. Karrai, and A. Imamoglu, Science **312**, 551 (2006).

[7] J. Berezovsky, M. Mikkelsen, N. Stoltz, L. Coldren, and D. Awschalom, Science **320**, 349 (2008).

[8] D. Press, T. D. Ladd, B. Zhang, and Y. Yamamoto, Nature (London) **456**, 218 (2008).

[9] D. Kim, S. E. Economou, S. C. Badescu, M. Scheibner, A. S. Bracker, M. Bashkansky, T. L. Reinecke, and D. Gammon, Phys. Rev. Lett. **101**, 236804 (2008).

[10] A. Greilich, S. E. Economou, S. Spatzek, D. Yakovlev, D. Reuter, A. Wieck, T. Reinecke, and M. Bayer, Nature Physics **5**, 262 (2009).

[11] E. D. Kim, K. Truex, X. D. Xu, B. Sun, D. G. Steel, A. S. Bracker, D. Gammon, and L. J. Sham, Phys. Rev. Lett. **104**, 167401 (2010).

[12] D. Kim, S. Carter, A. Greilich, A. Bracker, and D. Gammon, Nature Physics **7**, 223 (2011).

[13] A. Vamivakas, C. Lu, C. Matthiesen, Y. Zhao, S. Fält, A. Badolato, and M. Atatüre, Nature (London) **467**, 297 (2010).
[14] H. Kim, S. M. Thon, P. M. Petroff, and D. Bouwmeester, Appl. Phys. Lett. **95**, 243107 (2009).
[15] P. Fallahi, S. Yilmaz, and A. Imamoglu, Phys. Rev. Lett. **105**, 257402 (2010).
[16] A. Greilich, S. G. Carter, D. Kim, A. S. Bracker, and D. Gammon, Nature Photon **5**, 702 (2011).
[17] K. De Greve, P. L. McMahon, D. Press, T. D. Ladd, D. Bisping, C. Schneider, M. Kamp, L. Worschech, S. Hofling, A. Forchel *et al*., Nat Phys **7**, 872 (2011).
[18] H. J. Krenner, M. Sabathil, E. C. Clark, A. Kress, D. Schuh, M. Bichler, G. Abstreiter, and J. J. Finley, Phys. Rev. Lett. **94**, 57402 (2005).
[19] E. A. Stinaff, M. Scheibner, A. S. Bracker, I. V. Ponomarev, V. L. Korenev, M. E. Ware, M. F. Doty, T. L. Reinecke, and D. Gammon, Science **311**, 636 (2006).
[20] M. F. Doty, M. Scheibner, I. V. Ponomarev, E. A. Stinaff, A. S. Bracker, V. L. Korenev, T. L. Reinecke, and D. Gammon, Phys. Rev. Lett. **97**, 197202 (2006).
[21] M. Scheibner, M. F. Doty, I. V. Ponomarev, A. S. Bracker, E. A. Stinaff, V. L. Korenev, T. L. Reinecke, and D. Gammon, Phys. Rev. B **75**, 245318 (2007).
[22] D. Heiss, S. Schaeck, H. Huebl, M. Bichler, G. Abstreiter, J. J. Finley, D. V. Bulaev, and D. Loss, Phys. Rev. B **76**, 241306 (2007).
[23] B. D. Gerardot, D. Brunner, P. A. Dalgarno, P. Ohberg, S. Seidl, M. Kroner, K. Karrai, N. G. Stoltz, P. M. Petroff, and R. J. Warburton, Nature (London) **451**, 441 (2008).
[24] C.-Y. Hsieh, R. Cheriton, M. Korkusinski, and P. Hawrylak, Phys. Rev. B **80**, 243107 (2009).
[25] D. Brunner, B. D. Gerardot, P. A. Dalgarno, G. Wust, K. Karrai, N. G. Stoltz, P. M. Petroff, and R. J. Warburton, Science **325**, 70 (2009).
[26] T. M. Godden, S. J. Boyle, A. J. Ramsay, A. M. Fox, and M. S. Skolnick, Appl. Phys. Lett. **97**, 061113 (2010).
[27] T. Godden, J. Quilter, A. Ramsay, Y. Wu, P. Brereton, S. Boyle, I. Luxmoore, J. Puebla-Nunez, A. Fox, and M. Skolnick, Phys. Rev. Lett. **108**, 017402 (2012).
[28] C. Testelin, F. Bernardot, B. Eble, and M. Chamarro, Phys. Rev. B **79**, 195440 (2009).
[29] A. S. Bracker, M. Scheibner, M. F. Doty, E. A. Stinaff, I. V. Ponomarev, J. C. Kim, L. J. Whitman, T. L. Reinecke, and D. Gammon, Appl. Phys. Lett. **89**, 233110 (2006).
[30] J. I. Climente, M. Korkusinski, G. Goldoni, and P. Hawrylak, Phys. Rev. B **78**, 115323 (2008).
[31] C. Y. Lu, Y. Zhao, A. N. Vamivakas, C. Matthiesen, S. Fält, A. Badolato, and M. Atatüre, Phys. Rev. B **81**, 35332 (2010).
[32] M. F. Doty, J. I. Climente, M. Korkusinski, M. Scheibner, A. S. Bracker, P. Hawrylak, and D. Gammon, Phys. Rev. Lett. **102**, 47401 (2009).
[33] M. F. Doty, J. I. Climente, A. Greilich, M. Yakes, A. S. Bracker, and D. Gammon, J. Phys.: Conf. Ser. **245**, 012002 (2010).
[34] R. Roloff, T. Eissfeller, P. Vogl, and W. Pötz, New J. Phys. **12**, 093012 (2010).
[35] M. F. Doty, J. I. Climente, A. Greilich, M. Yakes, A. S. Bracker, and D. Gammon, Phys. Rev. B **81**, 035308 (2010).
[36] M. F. Doty, M. E. Ware, E. A. Stinaff, M. Scheibner, A. S. Bracker, I. V. Ponomarev, S. C. Badescu, V. L. Korenev, T. L. Reinecke, and D. Gammon, Physica Status Solidi B-Basic Solid State Physics **243**, 3859 (2006).
[37] I. V. Ponomarev, M. Scheibner, E. A. Stinaff, A. S. Bracker, M. F. Doty, S. C. Badescu, M. E. Ware, V. L. Korenev, T. L. Reinecke, and D. Gammon, Physica Status Solidi B-Basic Solid State Physics **243**, 3869 (2006).
[38] M. Scheibner, I. V. Ponomarev, E. A. Stinaff, M. F. Doty, A. S. Bracker, C. S. Hellberg, T. L. Reinecke, and D. Gammon, Phys. Rev. Lett. **99**, 197402 (2007).
[39] M. F. Doty, M. Scheibner, A. S. Bracker, and D. Gammon, Phys. Rev. B **78**, 115316 (2008).
[40] M. Scheibner, M. Yakes, A. S. Bracker, I. V. Ponomarev, M. F. Doty, C. S. Hellberg, L. J. Whitman, T. L. Reinecke, and D. Gammon, Nat. Phys. **4**, 291 (2008).
[41] A. Bennett, R. Patel, J. Skiba-Szymanska, C. Nicoll, I. Farrer, D. Ritchie, and A. Shields, Appl. Phys. Lett. **97**, 031104 (2010).
[42] A. Badolato, K. Hennessy, M. Atatüre, J. Dreiser, E. Hu, P. Petroff, and A. Imamoglu, Science **308**, 1158 (2005).
[43] M. Winger, A. Badolato, K. Hennessy, E. Hu, and A. Imamogùlu, Phys. Rev. Lett. **101**, 226808 (2008).
[44] A. Imamoglu, S. Fält, J. Dreiser, G. Fernandez, M. Atatüre, K. Hennessy, A. Badolato, and D. Gerace, J. Appl. Phys. **101**, 081602 (2007).
[45] D. Solenov, S. E. Economou, and T. L. Reinecke, arXiv:1204.5206.
[46] J. Planelles, J. Climente, F. Rajadell, M. F. Doty, A. S. Bracker, and D. Gammon, Phys. Rev. B **82**, 155307 (2010).
[47] D. Kim, W. Sheng, P. Poole, D. Dalacu, J. Lefebvre, J. Lapointe, M. Reimer, G. Aers, and R. Williams, Phys. Rev. B **79**, 045310 (2009).
[48] M. K. Yakes, C. D. Cress, J. G. Tischler, and A. S. Bracker, ACS Nano **4**, 3877 (2010).